# Convex Relaxation for Robust Vanishing Point Estimation in Manhattan World Supplementary Material

Bangyan Liao[1,2⋆], Zhenjun Zhao[3⋆], Haoang Li[4], Yi Zhou[5], Yingping Zeng[5], Hao Li[2], Peidong Liu[2✉]

[1]Zhejiang University [2]Westlake University
[3]The Chinese University of Hong Kong
[4]Hong Kong University of Science and Technology (Guangzhou)
[5]Hunan University

## Contents



In this supplementary material, we further discuss the following content:

- Theoretical proof of the global optimality of our proposed solvers in Sec. 4.2 and Sec. 4.3 of main paper (Sec. 1).
- Rounding and nearest rotation recovery implementation (Sec. 2).
- Additional experiment analysis of our solvers on the synthetic dataset (Sec. 3).
- Analysis of different RANSAC-based methods (Sec. 4).
- Additional experiment analysis of our solvers on the real-world dataset (Sec. 5).

## 1. Theoretical Proof

In this section, we provide a theoretical proof of two proposed SDP solvers.

⋆ Equal contribution.
✉ Corresponding author: Peidong Liu (liupeidong@westlake.edu.cn).

### 1.1. Preliminary Lemma

To begin with, define the multi block primal QCQP as:

$$\begin{aligned} \min_{\mathbf{x}_i \in \mathbb{R}^n} \quad & \sum_{i=1}^{l} \mathbf{x}_i^\top \mathbf{C}_i \mathbf{x}_i \\ \text{s.t.} \quad & \sum_{i=1}^{l} \mathbf{x}_i^\top \mathbf{A}_{ij} \mathbf{x}_i = b_j, \quad j = 1, \ldots, m. \end{aligned} \tag{Primal QCQP}$$

The Lagrange dual of primal QCQP can be derived as:

$$\begin{aligned} \max_{\mathbf{y} \in \mathbb{R}^m} \quad & \mathbf{b}^\top \mathbf{y} \\ \text{s.t.} \quad & \mathbf{C}_i - \sum_{j=1}^{m} y_j \mathbf{A}_{ij} \succeq 0, \quad i = 1, \ldots, l. \end{aligned} \tag{Dual SDP}$$

The dual of Lagrange dual of primal QCQP can be derived as:

$$\begin{aligned} \min_{\mathbf{X}_i \in \mathcal{S}^n} \quad & \sum_{i=1}^{l} \operatorname{trace}(\mathbf{C}_i \mathbf{X}_i) \\ \text{s.t.} \quad & \sum_{i=1}^{l} \operatorname{trace}(\mathbf{A}_{ij} \mathbf{X}_i) = b_j, \quad j = 1, \ldots, m \\ & \mathbf{X}_i \succeq \mathbf{0}, \quad i = 1, \ldots, l. \end{aligned} \tag{Dual Dual SDP}$$

Based on Lemma 2.1 in [4], we can define the following lemmas:

**Lemma 1.** Let $\mathcal{H}(\mathbf{y})_i = \mathbf{C}_i - \sum_{j=1}^{m} y_j \mathbf{A}_{ij}$. $\mathbf{x}$ is proved to be optimal for problem Primal QCQP, the strong duality holds between Primal QCQP and Dual SDP if there exists

$\mathbf{x}_i \in \mathbb{R}^n, \mathbf{y} \in \mathbb{R}^m$ satisfies:

$$\begin{cases} \sum_{i=1}^{l} \mathbf{x}_i^\top \mathbf{A}_{ij} \mathbf{x}_i = b_j, \ j = 1, \dots, m & \text{(Primal Feasibility)} \\ \mathcal{H}(\mathbf{y})_i \succeq 0, \ i = 1, \dots, l & \text{(Dual Feasibility)} \\ \mathcal{H}(\mathbf{y})_i \mathbf{x}_i = 0, \ i = 1, \dots, l & \text{(Stationary Condition)} \end{cases} \tag{1}$$

**Lemma 2.** In addition to Lemma 1, if $\mathcal{H}(\mathbf{y})_i$ has corank one, then all $\mathbf{x}_i \mathbf{x}_i^\top$ are the unique optimum of Dual Dual SDP and all $\mathbf{x}_i$ are the unique optimum of Primal QCQP.

Based on these two lemmas, we can prove the strong duality of our methods as follows.

### 1.2. Full SDP Problem

Let us first revisit Full SDP Problem as:

$$\begin{aligned} \min_{\mathbf{W}} \quad & \text{trace}(\mathbf{C}\mathbf{W}) \\ \text{s.t.} \quad & \mathbf{W}_{0,0} = \sum_{i=1}^{4} \mathbf{W}_{0,4(j-1)+i}, \quad j = 1, \dots, m, \\ & \mathbf{W}_{0,k} = \mathbf{W}_{k,k}, \quad k = 1, \dots, 4m, \\ & \text{trace}(\{\mathbf{W}_{0,0}\}_{i,j}) = \begin{cases} 1, & i = j \\ 0, & i \neq j \end{cases}, \quad \forall i, j \in \{1, 2, 3\}, \\ & \mathbf{W} \succeq \mathbf{0}, \end{aligned} \tag{Full SDP Problem}$$

where

$$\mathbf{W} \in \mathcal{S}_+^{10(1+4m) \times 10(1+4m)} = \begin{bmatrix} \mathbf{W}_{0,0} & \mathbf{W}_{0,1} & \dots & \mathbf{W}_{0,4m} \\ \mathbf{W}_{1,0} & \mathbf{W}_{1,1} & \dots & \mathbf{W}_{1,4m} \\ \vdots & \vdots & \ddots & \vdots \\ \mathbf{W}_{4m,0} & \mathbf{W}_{4m,1} & \dots & \mathbf{W}_{4m,4m} \end{bmatrix}. \tag{2}$$

**Theorem 1.** The duality gap of Full SDP Problem is zero under the noise-free and outlier-free condition. The Full SDP Problem solver guarantees that the optimal solution with rank 1.

*Proof:* Let we simplify the Full SDP Problem as:

$$\begin{aligned} \min_{\mathbf{W}} \quad & \text{trace}(\mathbf{C}\mathbf{W}) \\ \text{s.t.} \quad & \text{trace}(\mathbf{A}_1 \mathbf{W}) = 0, \quad j = 1, \dots, m, \\ & \text{trace}(\mathbf{A}_2 \mathbf{W}) = 0, \quad k = 1, \dots, 4m, \\ & \text{trace}(\mathbf{A}_3 \mathbf{W}) = 0, \\ & \text{trace}(\mathbf{A}_4 \mathbf{W}) = 1, \quad \text{trace}(\mathbf{A}_5 \mathbf{W}) = 1, \\ & \text{trace}(\mathbf{A}_6 \mathbf{W}) = 1, \\ & \mathbf{W} \succeq \mathbf{0}, \end{aligned} \tag{Full SDP Problem}$$

where the corresponding Lagrange multipliers defined as:

$$\mathbf{y} = \left[ \mathbf{y}_1 \in \mathbb{R}^m; \mathbf{y}_2 \in \mathbb{R}^{4m}; y_3; y_4; y_5; y_6 \right]. \tag{3}$$

Given the ground truth vanishing points $[\mathbf{d}_1^*; \mathbf{d}_2^*; \mathbf{d}_3^*]$ and permutation matrix $\mathbf{Q}^*$, we can derive the optimal $\boldsymbol{\omega}^*$ as:

$$\boldsymbol{\omega}^* = [\overline{\mathbf{D}}^*; \text{vec}(\mathbf{Q}^*) \otimes \overline{\mathbf{D}}^*], \tag{4}$$

where $\overline{\mathbf{D}}^* = [\mathbf{d}_1^*; \mathbf{d}_2^*; \mathbf{d}_3^*; 1]$ represents the homogeneous vector. Then, let $\mathbf{y} = \mathbf{0}$ become a zero vector. This implies that $\mathcal{H}(\mathbf{y}) = \mathbf{C}$ and $\boldsymbol{\omega}^{*\top} \mathcal{H}(\mathbf{y}) \boldsymbol{\omega}^* = \boldsymbol{\omega}^{*\top} \mathbf{C} \boldsymbol{\omega}^*$.

Since $\boldsymbol{\omega}^*$ satisfies our primal feasibility and $\mathbf{C}$ is diagonally symmetric, which implies $\mathcal{H}(\mathbf{y}) \succeq 0$. In addition, $\boldsymbol{\omega}^{*\top} \mathbf{C} \boldsymbol{\omega}^* = 0 \Longrightarrow \mathbf{C} \boldsymbol{\omega}^* = \mathbf{0}$. Thus the relaxation is tight according to Lemma 1. Since $\boldsymbol{\omega}$ is the only nonzero solution to $\boldsymbol{\omega}^\top \mathcal{H}(\mathbf{y}) \boldsymbol{\omega} = 0$ up to scale, according to our Lemma 2, our Full SDP Problem can always return the optimal solution. □

### 1.3. Single Block SDP Problem

Let us revisit Single Block SDP Problem as:

$$\begin{aligned} \min_{\mathbf{W}} \quad & \text{trace}(\mathbf{C}\mathbf{W}) \\ \text{s.t.} \quad & \mathbf{W}_{0,0,1} = \sum_{i=1}^{2} \text{trace}(\mathbf{W}_{0,j,i}), \quad j = 1, \dots, m, \\ & \mathbf{W}_{0,j,i} = \mathbf{W}_{j,j,i}, \quad \forall i \in \{1, 2\}, \quad j = 1, \dots, m, \\ & \text{trace}(\mathbf{W}_{0,0,1}) = 1, \quad \mathbf{W}_{0,0,1} = \mathbf{W}_{0,0,2}, \\ & \mathbf{W}_{*,*,i} \succeq \mathbf{0}, \quad \forall i \in \{1, 2\}, \end{aligned} \tag{Single Block SDP Problem}$$

where the tensor $\mathbf{W} \in \mathbb{R}^{3(m+1) \times 3(m+1) \times 2}$ with its block structure is defined as:

$$\mathbf{W}_{*,*,i} = \begin{bmatrix} \mathbf{W}_{0,0,i} & \mathbf{W}_{0,1,i} & \dots & \mathbf{W}_{0,m,i} \\ \mathbf{W}_{1,0,i} & \mathbf{W}_{1,1,i} & \dots & \mathbf{W}_{1,m,i} \\ \vdots & \vdots & \ddots & \vdots \\ \mathbf{W}_{m,0,i} & \mathbf{W}_{m,1,i} & \dots & \mathbf{W}_{m,m,i} \end{bmatrix}. \tag{5}$$

Besides, the auxiliary tensor $\mathbf{C} \in \mathbb{R}^{3(m+1) \times 3(m+1) \times 2}$ is defined as:

$$\begin{cases} \mathbf{C}_{*,*,1} = \text{diag}([\mathbf{0}_{3\times3}, \mathbf{n}_1 \mathbf{n}_1^\top, \dots, \mathbf{n}_m \mathbf{n}_m^\top]) \\ \mathbf{C}_{*,*,2} = \text{diag}([\mathbf{0}_{3\times3}, c^2 \mathbf{I}_3, \dots, c^2 \mathbf{I}_3]) \end{cases} \tag{6}$$

**Theorem 2.** The duality gap of Single Block SDP Problem is zero under the noise-free and outlier-free condition. The Single Block SDP Problem solver guarantees that the optimal solution with rank 1.

*Proof:* Let we simplify the single block QCQP as:

$$\begin{aligned} (\mathbf{x}_1^*, \mathbf{x}_2^*) = arg \min_{\mathbf{x}_1, \mathbf{x}_2} \quad & \mathbf{x}_1^\top \mathbf{C}_1 \mathbf{x}_1 + \mathbf{x}_2^\top \mathbf{C}_2 \mathbf{x}_2 \\ \text{s.t.} \quad & \mathbf{x}_1^\top \mathbf{A}_{1j} \mathbf{x}_1 = b_{1j}, \quad j = 1, \dots, m1, \\ & \mathbf{x}_2^\top \mathbf{A}_{2j} \mathbf{x}_2 = b_{2j}, \quad j = 1, \dots, m2, \\ & \mathbf{x}_1^\top \mathbf{A}_{3j1} \mathbf{x}_1 + \mathbf{x}_2^\top \mathbf{A}_{3j2} \mathbf{x}_2 = b_{3j}, \\ & \quad j = 1, \dots, m3. \end{aligned} \tag{7}$$

After setting all Lagrange multipliers to zero, we have $\mathcal{H}(\mathbf{y})_1 = \mathbf{C}_1$ and $\mathcal{H}(\mathbf{y})_2 = \mathbf{C}_2$, respectively. Since we assume that all lines are inliers, the ground truth $\mathbf{x}_1$ and $\mathbf{x}_2$ can be defined as:

$$\begin{aligned} \mathbf{x}_1^* &= [\mathbf{d}^*; \mathbf{d}^*; \dots; \mathbf{d}^*], \\ \mathbf{x}_2^* &= [\mathbf{d}^*; \mathbf{0}; \dots; \mathbf{0}], \end{aligned} \tag{8}$$

where $\mathbf{d}^*$ denotes the ground truth 3D line direction. The primal feasibility is always satisfied and the dual feasibility can be verified as:

$$\begin{aligned} 0 = \mathbf{x}_1^{*\top}\mathcal{H}(\mathbf{y})_1\mathbf{x}_1^* \leq \mathbf{x}_1^{\top}\mathcal{H}(\mathbf{y})_1\mathbf{x}_1, \\ 0 = \mathbf{x}_2^{*\top}\mathcal{H}(\mathbf{y})_2\mathbf{x}_2^* \leq \mathbf{x}_2^{\top}\mathcal{H}(\mathbf{y})_2\mathbf{x}_2, \\ \mathbf{x}_1^{\top}\mathbf{A}_{3j1}\mathbf{x}_1 + \mathbf{x}_2^{\top}\mathbf{A}_{3j2}\mathbf{x}_2 = b_{3j}. \end{aligned} \tag{9}$$

This equation can also verify the stationary condition. Since $\mathbf{x}_1^*$ and $\mathbf{x}_2^*$ are the only nonzero solutions of $\mathbf{x}^{\top}\mathcal{H}(\mathbf{y})_1\mathbf{x} = 0$ and $\mathbf{x}^{\top}\mathcal{H}(\mathbf{y})_2\mathbf{x} = 0$ up to scale, respectively. The Single Block SDP Problem can always return the optimal solution with rank 1. □

## 2. Rounding and Nearest Rotation Recovery

Due to observation noise and numerical approximation factors, the solutions obtained by the SDP optimizer may not strictly satisfy the rank-1 condition. Therefore, we need to employ a rounding strategy to recover from matrices approximated to rank 1. In addition, due to these approximate operations, the vanishing point matrix we obtain does not strictly adhere to the rotation matrix constraint. Hence, we need to employ a simple operation to restore the rotation matrix.

### 2.1. Rounding Procedure

Given a rank-1 approximation matrix $\mathbf{W} \in \mathbb{R}^{n\times n}$, the goal of the rounding operation is to obtain the optimal rank-1 approximation vector $\mathbf{w}$. We formulate the problem as follows:

$$\begin{aligned} \mathbf{w} = arg \min_{\mathbf{w}\in\mathbb{R}^n} \quad & \left\|\mathbf{w}\mathbf{w}^{\top} - \mathbf{W}\right\|_F^2 \\ \text{s.t.} \quad & \|\mathbf{w}\|_2^2 = 1. \end{aligned} \tag{10}$$

Utilizing the Frobenius norm, we can obtain an analytical solution that minimizes the norm error through Singular Value Decomposition (SVD) as:

$$\begin{aligned} \mathbf{U}\mathbf{\Sigma}\mathbf{V}^{\top} &= \text{SVD}(\mathbf{W}), \\ \mathbf{w} &= \sqrt{\sigma_1}[\mathbf{U}]_{*,1}, \end{aligned} \tag{11}$$

where $\sigma_1$ denotes the maximum singular value in $\mathbf{\Sigma} = \text{diag}(\sigma_1, \sigma_2, \sigma_3)$.

### 2.2. Closed-Form Nearest Rotation Estimation

Given a stacking rounding direction matrix $\mathbf{M} = [\mathbf{w}_1, \mathbf{w}_2, \mathbf{w}_3]$, the goal of the nearest rotation matrix estimation is to obtain a matrix $\mathbf{R} \in \mathbb{SO}(3)$ that satisfies the rotation matrix constraint with the minimum Frobenius norm error as:

$$\mathbf{R} = arg \min_{\mathbf{R}\in\mathbb{SO}(3)} \quad \|\mathbf{R} - \mathbf{M}\|_F^2 \tag{12}$$

Similarly, the closed-form solution can be obtained as:

$$\begin{aligned} \mathbf{U}\mathbf{\Sigma}\mathbf{V}^{\top} &= \text{SVD}(\mathbf{M}), \\ \mathbf{R} &= \mathbf{U}\mathbf{\Sigma}^{'}\mathbf{V}^{\top}, \end{aligned} \tag{13}$$

where $\mathbf{\Sigma}^{'} = \text{diag}(1, 1, \det(\mathbf{U}\mathbf{V}^{\top}))$.

## 3. Additional Synthetic Experiments

**Complete accuracy comparisons across outlier ratios.** We show the complete accuracy results across outlier ratios in Fig. 1. While only the $F_1$-score is shown in Sec. 5.1.2, this figure includes precision and recall as well. ***GlobustVP*** consistently demonstrates superior robustness and accuracy across varying outlier ratios.

**Accuracy comparisons across noise levels.** We fix the number of lines at 60 and the outlier ratio at 20%, while varying the standard deviation of zero-mean Gaussian noise from 1 to 5 pixels. All statistical analyses are performed over 40 independent Monte Carlo trials. Fig. 2 shows the precision, recall, and $F_1$-score as the noise level increases. Recall and $F_1$-score reveal that **RANSAC**, **J-Linkage**, **T-Linkage**, and **Quasi-VP** are highly sensitive to noise. **BnB** begins to degrade significantly when the noise reaches 4 pixel of noise. In contrast, ***GlobustVP*** maintains consistent performance across varying noise levels.

**Complete accuracy and efficiency comparisons across line counts.** In Sec. 5.1.2 of main paper, we present comparisons of ***GlobustVP*** with **RANSAC** and **BnB** only. Here, we provide the complete accuracy and efficiency results for all methods. Fig. 3 shows the $F_1$-score and runtime concerning the increasing number of lines with all methods. ***GlobustVP*** demonstrates consistent performance on both accuracy and efficiency as the number of lines increases.

**Ablation study on uncertainty.** Following [6–8], we derive the uncertainty for each line segment and incorporate it into $(\mathbf{d}^{\top}\mathbf{n})^2$. We conduct an ablation study to evaluate its impact on accuracy (*i.e.*, $F_1$-score) across 500 independent Monte Carlo trials with 60 lines. We vary the noise levels while keeping the outlier ratio fixed at 20%, and vary the outlier ratio while fixing the noise level at $\sigma = 3$. As shown in Fig. 4, incorporating uncertainty slightly improves performance, while our original method (*i.e.*, w/o uncertainty) achieves comparable results.

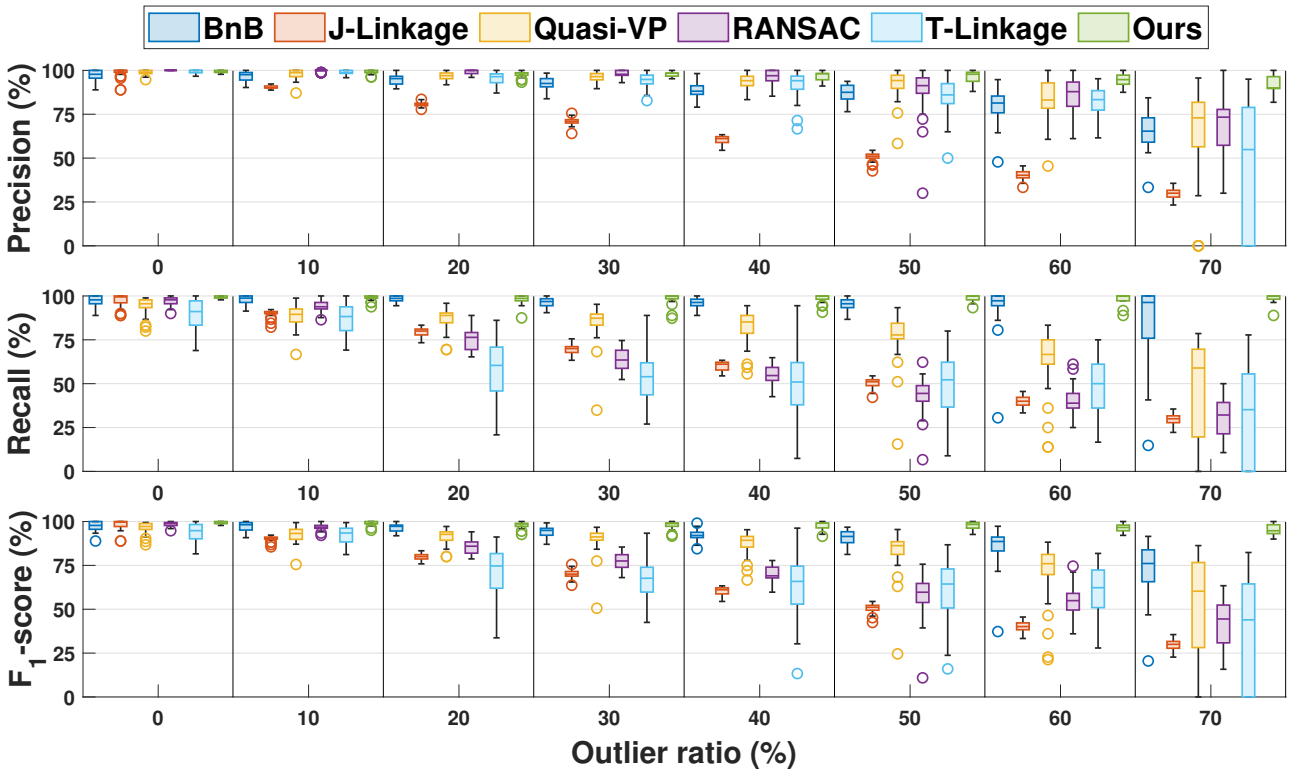


Figure 1. Accuracy comparisons on the synthetic dataset with respect to the outlier ratios: boxplots of precision (top), recall (middle), and $F_1$-score (bottom). Best viewed in color and high resolution.

## 4. Analysis of RANSAC-Based Methods

In Sec. 5.1 of main paper, we use a RANSAC-based method [14] (denoted as **RANSAC**) as a baseline for comparison with ***GlobustVP***. The setup includes a maximum of 1,000 iterations, ensuring a 0.99 confidence level that a subset comprised solely of inliers is selected.

To ensure a fair and comprehensive comparison, we further analyze the performance of **RANSAC** and its variants. Specifically, we include two RANSAC variants: a slower version (denoted as **RANSAC-10K**), which allows up to 10,000 iterations to match the runtime of ***GlobustVP***, and **MAGSAC** [1, 2], a state-of-the-art RANSAC-based method designed to improve accuracy.

We evaluate these methods on the YUD [5] and SU3 [15] datasets, using the AA metric described in Sec. 5.2.1 of main paper. As shown in Tab. 1, **RANSAC** achieves the fastest runtime due to its limited iterations, but its accuracy is significantly lower compared to the other methods. **RANSAC-10K** improves accuracy over **RANSAC** on all metrics, albeit at the cost of increased runtime. On SU3 [15], **MAGSAC** surpasses **RANSAC-10K** in accuracy on all angular thresholds while consuming slightly more time. However, on YUD [5], **RANSAC-10K** outperforms **MAGSAC** in AA@3° and AA@10°.

Our proposed ***GlobustVP*** consistently outperforms all RANSAC-based methods on YUD [5] across all accuracy metrics. On SU3 [15], ***GlobustVP*** demonstrates superior performance in AA@3° and AA@5° while slightly lagging behind **MAGSAC** in AA@10°. These results highlight the balanced trade-off between accuracy and runtime efficiency achieved by ***GlobustVP*** across both YUD [5] and SU3 [15] datasets.

| Dataset | Method | AA@3° ↑ | AA@5° ↑ | AA@10° ↑ | Time (ms) ↓ |
|---|---|---|---|---|---|
| YUD [5] | RANSAC [14] | 53.3 | 64.7 | 78.4 | 9.0 |
| | RANSAC-10K [14] | 56.1 | 70.6 | 82.4 | 48.8 |
| | MAGSAC [1] | 52.6 | 73.2 | 81.7 | 12.4 |
| | GlobustVP (Ours) | **67.6** | **87.3** | **96.1** | **48.8** |
| SU3 [15] | RANSAC [10] | 48.2 | 74.0 | 82.8 | 9.0 |
| | RANSAC-10K [10] | 70.6 | 80.4 | 86.2 | 48.8 |
| | MAGSAC [1] | 76.2 | 84.6 | 92.8 | 9.2 |
| | GlobustVP (Ours) | **80.2** | **86.8** | **92.4** | **48.8** |

Table 1. Angular accuracy and runtime comparisons of RANSAC-based methods and ***GlobustVP*** on YUD [5] and SU3 [15] datasets. The best and second-best performance for each metric are highlighted.

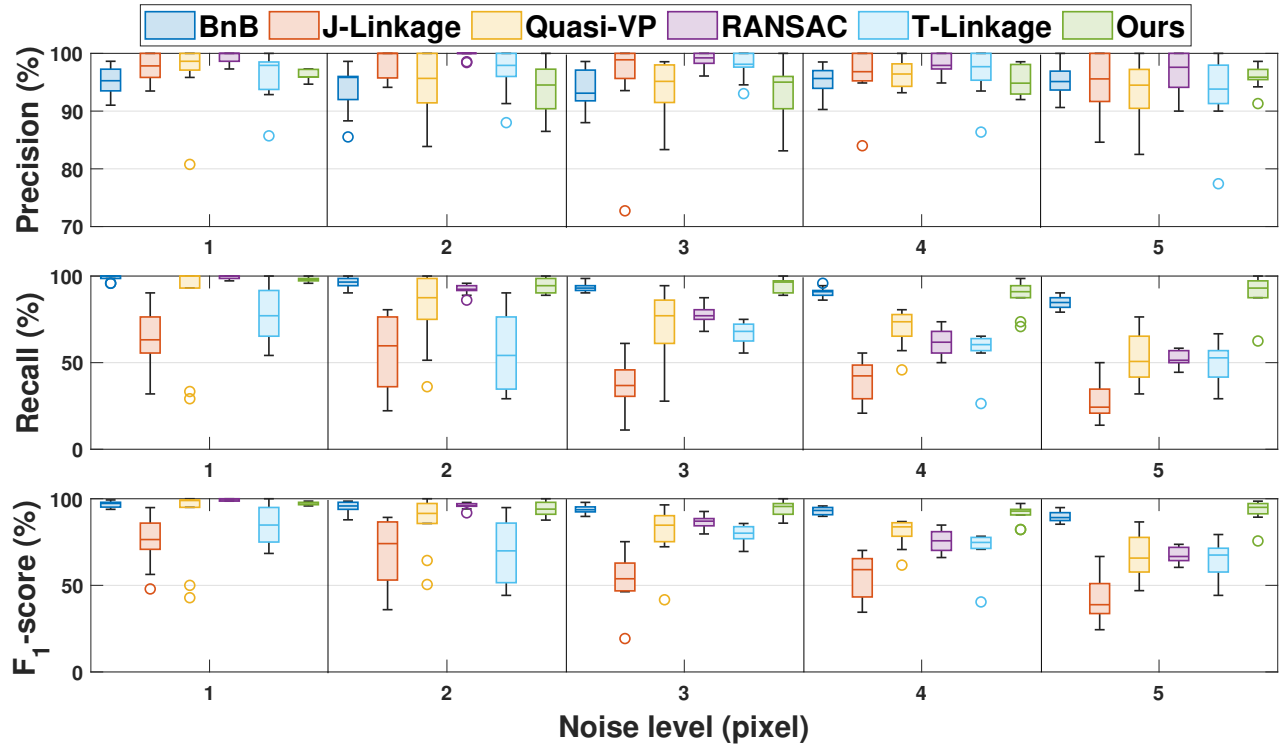


Figure 2. Accuracy comparisons on the synthetic dataset with respect to the noise levels: boxplots of precision (top), recall (middle), and $F_1$-score (bottom). Best viewed in color and high resolution.

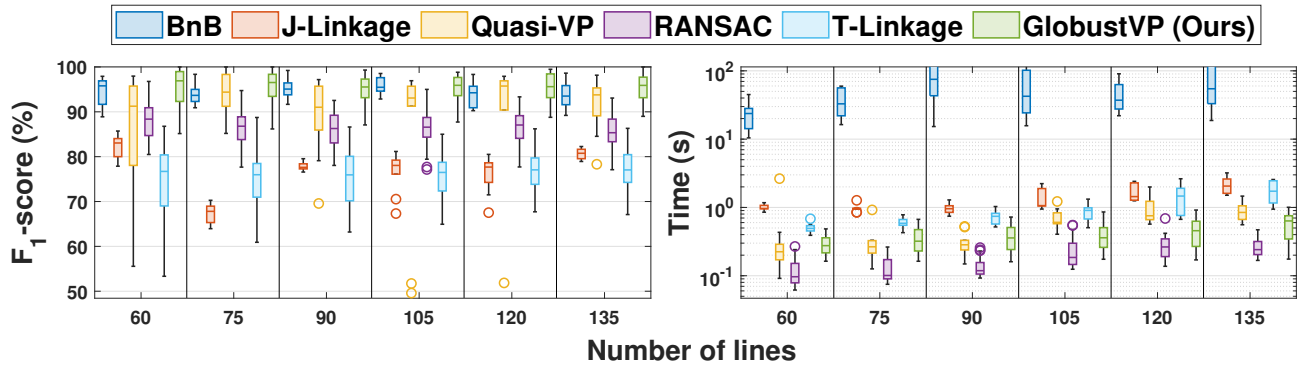


Figure 3. Accuracy and efficiency comparisons of all baseline methods on the synthetic dataset with respect to the number of image lines. Best viewed in color and high resolution.

## 5. Additional Real-World Experiments

### 5.1. York Urban Database

**Accuracy comparisons.** We provide a quantitative comparison of the baseline methods on YUD [5] in terms of $F_1$-score and consistency error, as shown in Fig. 5. We observe that **RANSAC**, **J-Linkge**, and **T-Linkage** struggle to achieve satisfactory accuracy, with up to 30% images displaying a sub-optimal $F_1$-score (below 90%) and a large consistency error exceeding 2.25 pixels. While **BnB** demonstrates notable accuracy, it encounters convergence issues on a subset of images, leading to sub-optimal solutions. The performance of **Quasi-VP** falls between that of **RANSAC** and **BnB**, providing only a moderate level of accuracy. In contrast, ***GlobustVP*** achieves the highest accuracy by leveraging a global solver technique. Furthermore, to evaluate the accuracy of vanishing point estimation, we follow [6] and compute the angular differences between the estimated and the ground truth dominant direc-

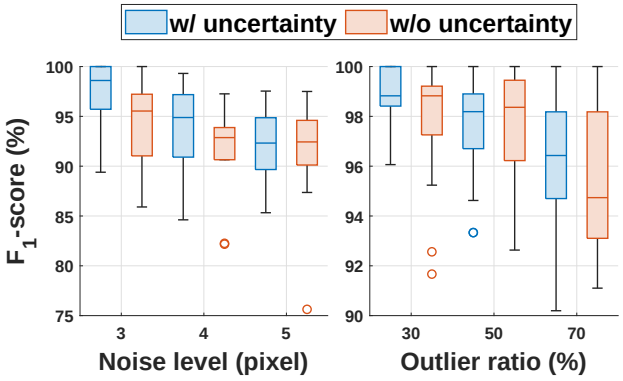


Figure 4. Comparisons of our method with (w/) and without (w/o) incorporating uncertainty. Best viewed in color.

tions. The corresponding histogram of the angular differences on YUD [5] is shown in Fig. 6. The results demonstrate that approximately $50\%$ of the estimated dominant directions have angular difference less than $2^\circ$. This demonstrates that ***GlobustVP*** achieves excellent angular accuracy in vanishing point estimation.

**Additional representative comparisons.** We provide additional representative evaluation results on YUD [5] using the manually extracted image lines with 2 and 3 vanishing points (VPs), as shown in Fig. 7. Furthermore, to further demonstrate the performance of ***GlobustVP*** on real-world images, we use YUD [5] and apply the Line Segment Detector (LSD) [13] to extract image lines. Subsequently, we estimate vanishing points using various methods and evaluate their accuracy. It is important to note that the extracted image lines inherently contain some outliers. The results in Fig. 8 demonstrate a performance degradation of previous methods compared to those using manually extracted image lines. Specifically, while **RANSAC** achieves a higher recall ($86.17\%$) due to its larger number of inliers, it also generates a greater number of incorrectly clustered lines, with a precision rate of $60.00\%$. Furthermore, **BnB** shows sub-optimal recall performance, as previously discussed in [10]. In contrast, both **Quasi-VP** and ***GlobustVP*** achieve a balanced performance in terms of precision and recall. Notably, ***GlobustVP*** exhibits lower consistency error than other approaches, due to its inherent global optimality.

### 5.2. NYU-VP Dataset

To further evaluate the performance of ***GlobustVP***, we conduct additional experiments on the NYU-VP dataset [9]. The dataset contains ground truth vanishing points for 1449 indoor scenes, with line segments extracted from the images using LSD [13]. The results shown in Fig. 9 demonstrate that ***GlobustVP*** produces a higher number of inliers than previous approaches.

## References


[1] Daniel Barath, Jiri Matas, and Jana Noskova. Magsac: marginalizing sample consensus. In *CVPR*, pages 10197–10205, 2019. 4

[2] Daniel Barath, Jana Noskova, Maksym Ivashechkin, and Jiri Matas. Magsac++, a fast, reliable and accurate robust estimator. In *CVPR*, pages 1304–1312, 2020. 4

[3] Jean Charles Bazin, Yongduek Seo, Cédric Demonceaux, Pascal Vasseur, Katsushi Ikeuchi, In-So Kweon, and Marc Pollefeys. Globally optimal line clustering and vanishing point estimation in manhattan world. In *CVPR*, pages 638–645, 2012. 8, 9

[4] Diego Cifuentes, Sameer Agarwal, Pablo A Parrilo, and Rekha R Thomas. On the local stability of semidefinite relaxations. *Mathematical Programming*, pages 1–35, 2022. 1

[5] Patrick Denis, James H. Elder, and Francisco J. Estrada. Efficient edge-based methods for estimating manhattan frames in urban imagery. In *ECCV*, 2008. 4, 5, 6, 7, 8, 9

[6] Wolfgang Förstner. Optimal vanishing point detection and rotation estimation of single images from a legoland scene. In *Proc. ISPRS Commission III Symp. Photogramm. Comput. Vis. Image Anal*, pages 157–162, 2010. 3, 5

[7] Wolfgang Förstner and Bernhard P Wrobel. *Photogrammetric computer vision*. Springer, 2016.

[8] Stephan Heuel and Wolfgang Forstner. Matching, reconstructing and grouping 3d lines from multiple views using uncertain projective geometry. In *CVPR*, 2001. 3

[9] Florian Kluger, Eric Brachmann, Hanno Ackermann, Carsten Rother, Michael Ying Yang, and Bodo Rosenhahn. Consac: Robust multi-model fitting by conditional sample consensus. In *CVPR*, pages 4633–4642, 2020. 6, 9

[10] Haoang Li, Ji Zhao, Jean Charles Bazin, and Yunhui Liu. Quasi-globally optimal and near/true real-time vanishing point estimation in manhattan world. *IEEE TPAMI*, 44: 1503–1518, 2020. 6, 8, 9

[11] Luca Magri and Andrea Fusiello. T-linkage: A continuous relaxation of j-linkage for multi-model fitting. In *CVPR*, pages 3954–3961, 2014. 8

[12] Roberto Toldo and Andrea Fusiello. Robust multiple structures estimation with j-linkage. In *ECCV*, 2008. 8

[13] Rafael Grompone von Gioi, Jérémie Jakubowicz, Jean-Michel Morel, and Gregory Randall. Lsd: A fast line segment detector with a false detection control. *IEEE TPAMI*, 32:722–732, 2010. 6, 9

[14] Lilian Zhang, Huimin Lu, Xiaoping Hu, and Reinhard Koch. Vanishing point estimation and line classification in a manhattan world with a unifying camera model. *IJCV*, 117:111–130, 2016. 4, 8, 9

[15] Yichao Zhou, Haozhi Qi, Yuexiang Zhai, Qi Sun, Zhili Chen, Li-Yi Wei, and Yi Ma. Learning to reconstruct 3d manhattan wireframes from a single image. In *ICCV*, pages 7698–7707, 2019. 4

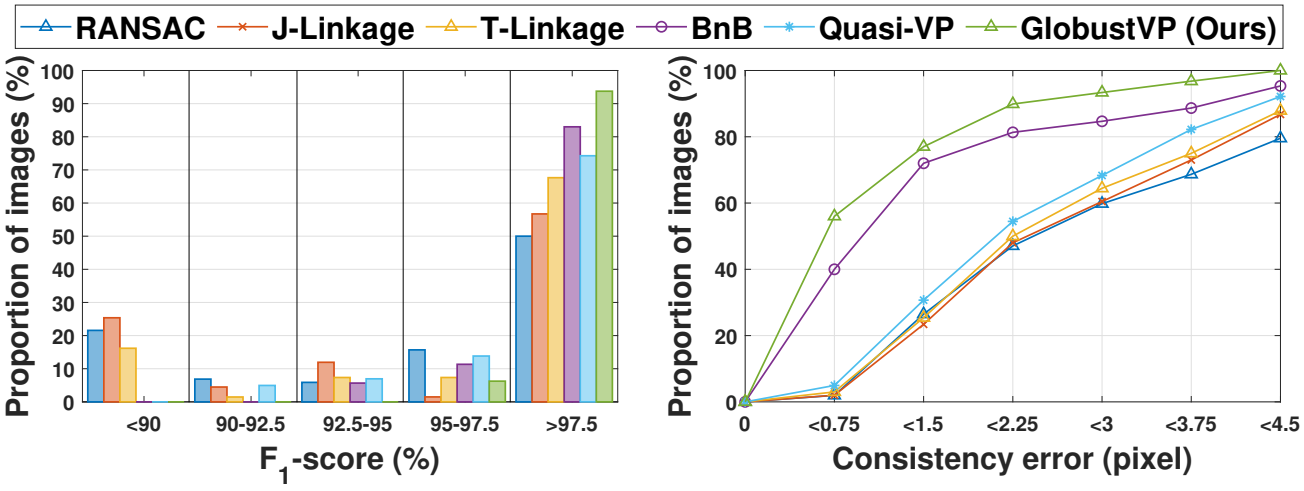


Figure 5. Accuracy comparisons on all images of YUD [5] using the manually extracted image lines. *Left:* $F_1$-score of line-VP association. *Right:* Cumulative histogram of the consistency error. Best viewed in color.

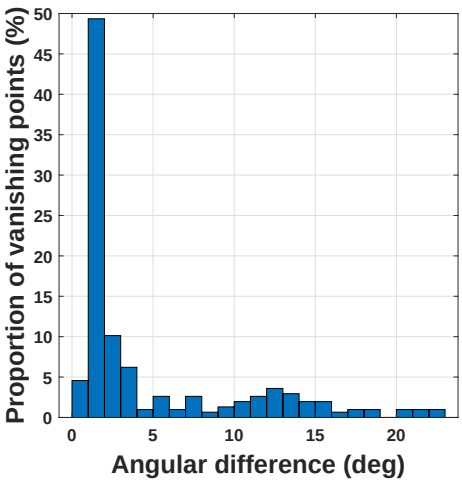


Figure 6. Histogram of angular differences between the estimated and the ground truth dominant directions on YUD [5].

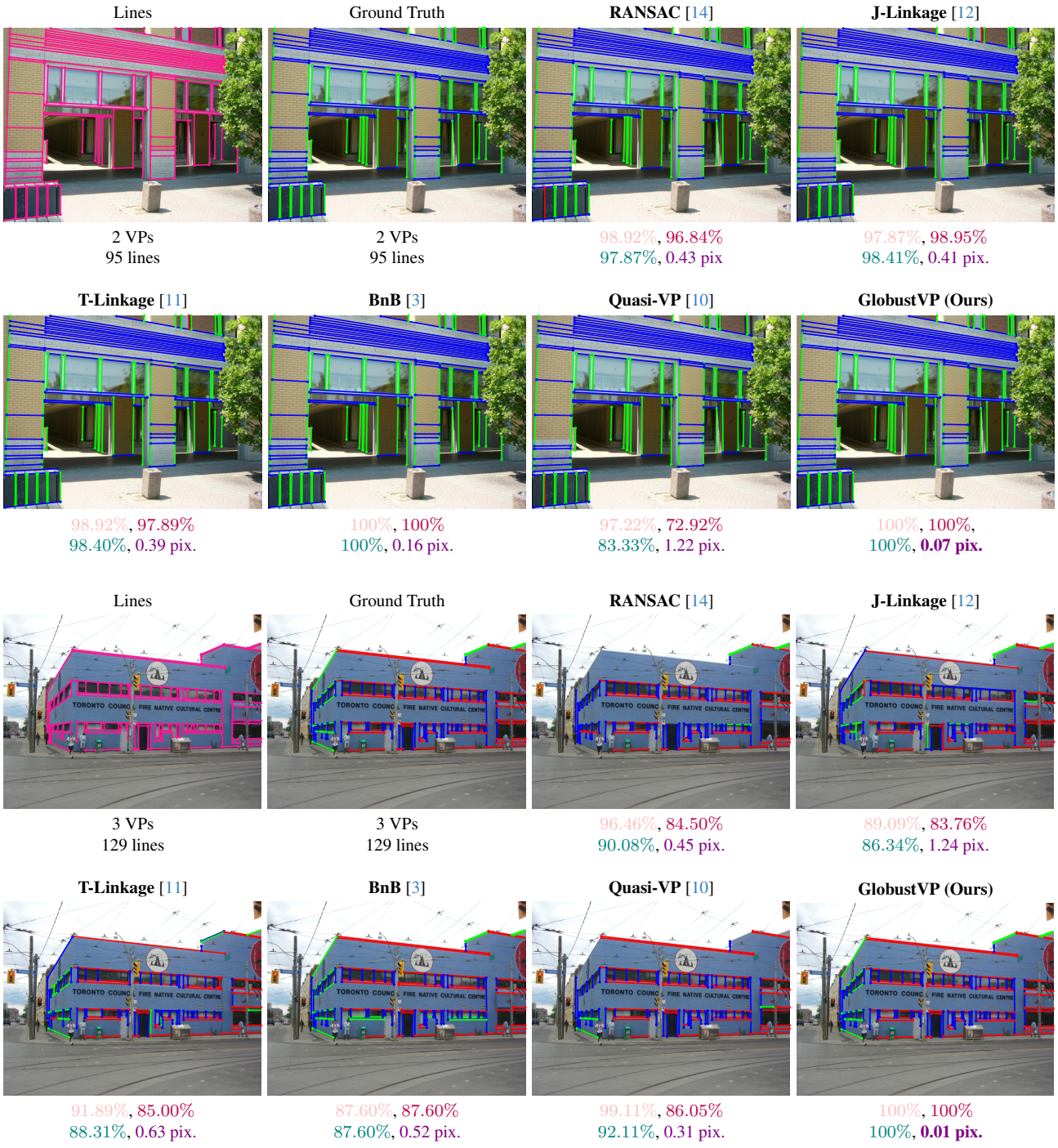


Figure 7. Representative comparisons on YUD [5] using the manually extracted image lines. Different line-VP associations are shown in respective colors. The numbers below each image represent the respective precision ↑, recall ↑, $F_1$-score ↑, and consistency error ↓ of line-VP association. Best viewed in color and high resolution.

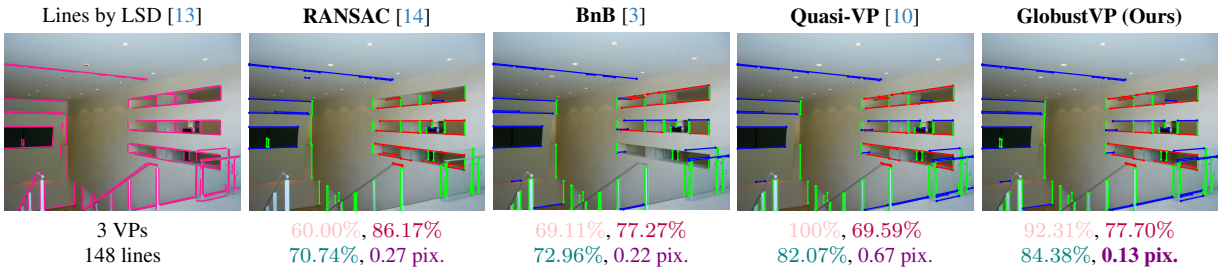


Figure 8. Representative comparisons on YUD [5] using the automatically extracted image lines by LSD [13]. Different line-VP associations are shown in respective colors. The numbers below each image represent the respective precision ↑, recall ↑, $F_1$-score ↑, and consistency error ↓ of line-VP association. Best viewed in color and high resolution.

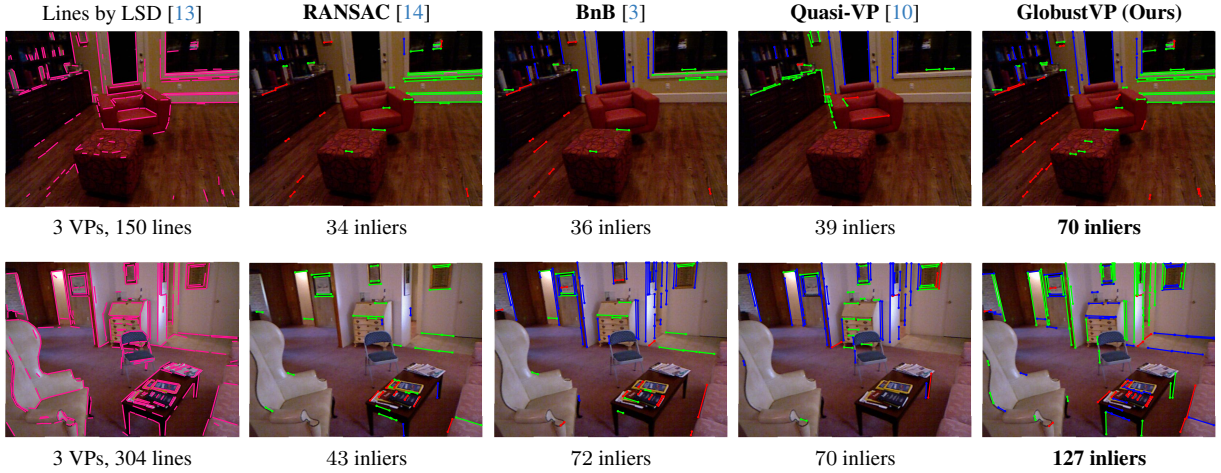


Figure 9. Representative comparisons on NYU-VP dataset [9] using the automatically extracted image lines by LSD [13]. Different line-VP associations are shown in respective colors. The number below each image represents the number of inliers identified by each method. Best viewed in color and high resolution.